Journal of Materials Chemistry A

ROYAL SOCIETY OF CHEMISTRY

PAPER

View Article Online
View Journal | View Issue

Cite this: J. Mater. Chem. A, 2021, 9, 22440

Ge 4s^2 lone pairs and band alignments in GeS and GeSe for photovoltaics†

Matthew J. Smiles,[a] Jonathan M. Skelton, *[b] Huw Shiel,[a] Leanne A. H. Jones, [a] Jack E. N. Swallow,‡[a] Holly J. Edwards,[a] Philip A. E. Murgatroyd,§[a] Thomas J. Featherstone,[a] Pardeep K. Thakur, [c] Tien-Lin Lee,[c] Vinod R. Dhanak[a] and Tim D. Veal *[a]

Received 14th July 2021
Accepted 17th September 2021

DOI: 10.1039/d1ta05955f

rsc.li/materials-a

Germanium sulfide and germanium selenide bulk crystals were prepared using a melt growth technique. X-ray photoemission spectroscopy (XPS) was used to determine ionisation potentials of 5.74 and 5.48 eV for GeS and GeSe respectively. These values were used with the previously-measured band gaps to establish the natural band alignments with potential window layers for solar cells and to identify CdS and TiO_2 as sensible choices. The ionisation potential of GeS is found to be smaller than in comparable materials. Using XPS and hard X-ray photoemission (HAXPES) measurements in conjunction with density-functional theory calculations, we demonstrate that stereochemically active Ge 4s lone pairs are present at the valence-band maxima. Our work thus provides direct evidence for active lone pairs in GeS and GeSe, with important implications for the applications of these and related materials such as Ge-based perovskites.

1 Introduction

Modern photovoltaics (PV) research aims to challenge crystalline silicon as the dominant material in the industry. Thin film cadmium telluride (CdTe) has been a major success in achieving an efficiency of 22.1%, similar to silicon.[1] However, there are issues with CdTe, including concerns regarding the toxicity of cadmium and the scarcity of tellurium, the latter of which in particular will limit the extent to which CdTe can meet the challenge of scaling up PV for terawatt energy generation.[2,3]

One non-toxic and earth-abundant material that has shown great potential is antimony selenide (Sb_2Se_3). With its exemplary optical properties, Sb_2Se_3 solar cells have achieved a record efficiency of 9.2% in a decade despite the limited number of groups working on the material.[4,5] Part of the success is down to its orthorhombic *Pnma* crystal structure which comprises nanoribbons held together by van der Waals interactions. Theoretical and experimental studies show strong conductivity parallel to the ribbons, a benefit for PV applications if the growth orientation can be controlled.[6,7]

1.1 Materials with active lone pairs

An important feature of Sb_2Se_3 is the contribution of the Sb 5s^2 lone pair to the valence band.[9] Materials with stereochemically active lone pairs are attracting growing interest because of the high power conversion efficiency of methyl-ammonium lead iodide (MAPI) solar cells.[1] There is growing evidence to suggest that a large part of the high performance of this material is due to the Pb 6s^2 lone pair, which is thought to underpin some of its desirable PV properties.[10,11] The antibonding states in the VBM should lead to shallow rather than deep states, the formation of benign grain boundaries, and strong defect tolerance. The 6s^2 orbital also results in band edges with greater dispersion, leading to smaller carrier effective masses and enhanced carrier mobility, both of which are desirable for PV applications.[12]

1.2 GeS and GeSe photovoltaics

Germanium sulfide (GeS) and germanium selenide (GeSe) share a lot of the same properties as Sb_2Se_3. Ge is less toxic than both Sb and Cd. Ge is also over six times more Earth-abundant than Sb and Cd, and both S and Se are considerably more abundant than Te.[13] Both GeS and GeSe have good optical properties, with

[a]Stephenson Institute for Renewable Energy and Department of Physics, University of Liverpool, Liverpool, L69 7ZF, UK. E-mail: T.Veal@liverpool.ac.uk
[b]Department of Chemistry, University of Manchester, Oxford Road, Manchester, M13 9PL, UK. E-mail: jonathan.skelton@manchester.ac.uk
[c]Diamond Light Source Ltd., Harwell Science and Innovation Campus, Didcot, Oxfordshire OX11 0DE, UK

† Electronic supplementary information (ESI) available: Valence band photoemission data over expanded energy ranges, X-ray diffraction measurements of GeS, additional core-level measurements and fitting, calculated pDoS curves with no cross-section corrections or broadening applied, and a comparison of calculation results with and without Ge 3d states treated as valence electrons. See DOI: 10.1039/d1ta05955f

‡ Present address: Department of Materials, University of Oxford, Oxford, UK.
§ Present address: Department of Physics, University of St. Andrews, St. Andrews, UK.

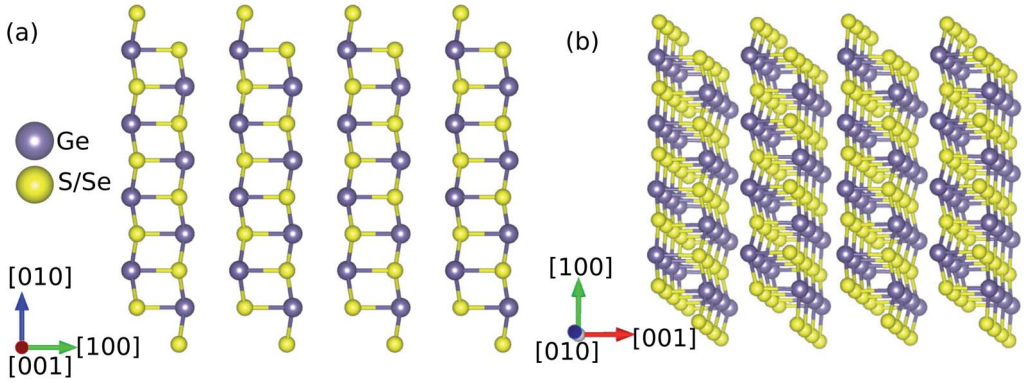

Fig. 1 Crystal structure of GeS/GeSe (a) along the [001] direction and (b) rotated slightly to highlight the nanosheets. The structure of both materials are orthorhombic with the *Pnma* space group. These images were prepared using the VESTA software.[8]

band gaps in the ideal range according to the detailed balance limit.[14–16] While GeS and GeSe share the same *Pnma* space group as Sb_2Se_3, they have covalent bonds in two directions, creating sheets rather than ribbons, with van der Waals interactions along the other direction (Fig. 1(a) and (b)). As noted above, studies on Sb_2Se_3 suggest strong conductivity in the direction of the covalent bonds but weak conductivity in the directions of the van der Waals interactions. Having covalent bonds along two directions could therefore be beneficial for cell design, whilst also benefiting from the benign grain boundaries. Finally, Ge is in the +2 oxidation state in both GeS and GeSe and adopts a distorted local structure, which suggests the cations may have stereochemically active lone pairs.[17–19] These properties, along with the recently reported 1.36% and 5.2% power conversion efficiency for a GeS and GeSe solar cell, respectively,[20,21] demonstrate the potential of these materials.

1.3 Identifying ns^2 lone pair states using photoemission spectroscopy

To probe the Ge 4s lone pair states, hard X-ray photoemission spectroscopy (HAXPES, $h\nu = 5.921$ keV) and lab-based X-ray photoemission spectroscopy (XPS, $h\nu = 1.487$ keV) were used. By utilising more than one photon energy, the energy dependence of the photoionisation cross sections (*i.e.* the probabilities of an electron being emitted from its electronic state) can be exploited. The cross sections of the valence and semi-core orbitals in GeS and GeSe as a function of energy are presented in Fig. 2, with vertical dotted lines indicating the energies used for measurements in this study.[22]

As can be seen in Fig. 2, the s-orbital cross-sections decrease more gradually relative to other orbitals as the photon energy increases, which is due to them being more contracted.[23] This in turn implies that s orbitals will be relatively more prominent in HAXPES than in XPS spectra, as they will contribute a higher proportion of the total intensity at a higher incident photon energy, as found in previous studies on materials with ns^2 lone pairs.[9,17,24,25] HAXPES can also offer higher spectral resolution, but also has reduced surface sensitivity compared to XPS, so there are merits to using both techniques.

1.4 Determination of band alignments

An advantage of a laboratory – as opposed to synchrotron – photoemission system is that it allows for measurement of the

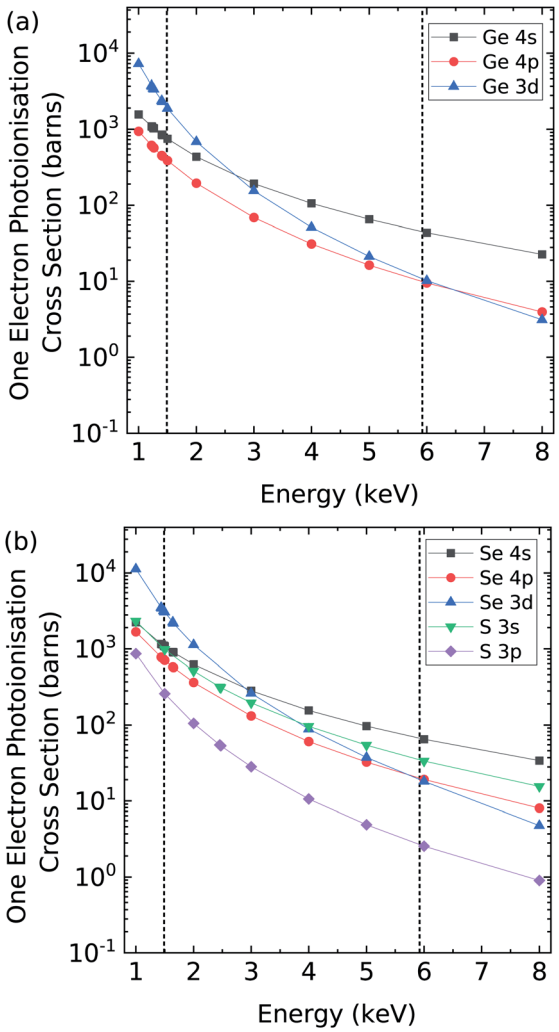

Fig. 2 One-electron photoionisation cross sections of (a) Ge and (b) S and Se.[22] The vertical lines at 5.921 keV and 1.487 keV show the energies used for our HAXPES and XPS measurements, respectively.

secondary electron cut-off (SEC) to determine the ionisation potential, and, therefore, the absolute position of the valence band maximum (VBM) with respect to the vacuum level. By measuring the band gap, it is then also possible to determine the position of the conduction band minimum (CBM).

The conduction band offset (CBO) between the window layer and absorber layer is an important factor in the performance of PV devices.[26,27] If the offset is positive, the conduction band of the window layer is higher than the absorber layer, and a 'spike-like' barrier forms which opposes the drift of excited electrons from absorber to window layer and thus limits the short-circuit current of the device. If, however, the offset is negative, and the conduction band (CB) of the window layer is lower than that of the absorber layer, a 'cliff-like' barrier is formed. This can lead to recombination at the interface between the conduction and valence bands and a lower built-in voltage, producing a lower open-circuit voltage. Valence band spectra, alongside the SEC and density-functional theory (DFT) calculations, can additionally be used to analyse the composition of the valence band (VB) and thus to determine the impact of different atomic states on the ionisation potential.[9,28]

1.5 Previous characterisation of Ge active lone pairs

Early studies on GeS and GeSe identified three key features in the valence band spectrum named peaks I, II and III (Fig. S1†). It was suggested that peak I was composed of S 3p/Se 4p and Ge 4p orbitals, peak II of Ge 4s orbitals, and peak III of S 3s/Se 4s states.[29–41] This appears to be based on early speculation linked to the lead chalcogenides that was subsequently propagated in much of the literature. Waghmare *et al.* performed calculations on IV–VI chalcogenides in the cubic (rocksalt) structure and demonstrated that Ge 4s states are also present in peak I at the VBM.[42] Since then, theoretical calculations of orthorhombic GeS have also indicated the presence of Ge 4s states at the VBM, but other studies of GeS are limited to monolayers and amorphous materials, the electronic structures of which differ significantly from the electronic structures of bulk crystals.[43–46] Theoretical calculations on orthorhombic GeSe have also suggested that the Ge 4s orbitals contribute to the VBM, with one study loosely comparing the calculated density of states to XPS measurements of the valence band spectra.[20,47,48] GeS and GeSe are known to adopt distorted crystal structures,[49] and theoretical studies on both have demonstrated the asymmetric electron densities expected in materials with stereochemically active lone pairs.[43,46,50] However, neither material has been studied using HAXPES, and this would be the most effective method for confirming (or otherwise) the presence of Ge 4s states at the VBM.

Beyond the germanium chalcogenides, studies of Ge 4s lone pairs remain limited. While Ge(II) would appear to be an alternative to Pb(II), in perovskite materials it has largely been overlooked due to the lower binding energy of the Ge 4s electrons compared to the Sn 5s and Pb 6s electrons.[51] Mitzi has previously shown that in crystals of $(C_4H_9NH_3)_2MI_4$ perovskites (M = Ge, Sn, Pb) the stereochemical activity of the lone pair was strongest in the Ge materials.[52] Despite this, it is generally accepted that the lone s orbital becomes more stable on descending the group (*i.e.* $6s^2$ lone pairs are more stable than $4s^2$ lone pairs),[11] and this decreased stability does mean that Ge perovskites are more prone to oxidation, which further explains the limited studies on these materials.[10] However, with careful preparation, Ge perovskites with stereochemically active lone pairs could prove useful in the development of tandem solar cells given their wide band gaps. A proof of concept study of single-junction Ge perovskite cells has been performed, albeit with a limited efficiency of 0.2%.[53] It has been further demonstrated that other Ge perovskite materials can be made, with multiple studies reporting the successful preparation of crystals of the $CsGeX_3$ (X = Cl, Br, I) perovskite series.[54–57] Theoretical studies of $CsGeI_3$, $(CH_3NH_3)GeCl_3$ and $(CH_3NH_3)GeI_3$ have all shown a contribution from the Ge 4s orbitals to the VBM, again suggesting stereochemically active lone pairs.[53,57–59]

1.6 Present study

We have prepared GeS and GeSe crystals using a melt-growth technique and performed HAXPES and XPS measurements performed to investigate the electronic structures. We combine SEC measurements were with the valence band spectra and previously-reported band gaps to determine the ionisation potentials, and we compare the band edge positions to related materials and to common solar cell window layers. Finally, we also model the valence band spectra using DFT calculations to establish the role of the different orbitals in determining the electronic structure, band levels, and band alignments. This combination of photoemission measurements and theoretical modelling allows us to unambiguously confirm the presence of active Ge lone pairs in GeS and GeSe, which has implications for the PV and other applications of these and related systems.

2 Experimental and computational details

Bulk crystals of GeS and GeSe were prepared using a melt-growth technique. Stoichiometric amounts of Ge and S or Se (all with 5N purity, Alfa Asear) were sealed in an evacuated quartz tube at a pressure $\leq 10^{-4}$ Torr. For GeS this was 2.0813 g of Ge and 0.9187 g of S and for GeSe this was 1.4373 g of Ge and 1.5627 g of Se. The mixtures were melted at 800 °C for 24 hours, then slowly cooled to 500 °C, where the mixture was held for 100 hours before finally being cooled to room temperature.

Material characterisation was performed using X-ray diffraction (XRD). XRD measurements were taken under ambient conditions using a Rigaku Smartlab X-ray diffractometer equipped with a rotating copper anode. Monochromated $K\alpha_1$ incident radiation was used to perform θ:2θ scans between 20° and 80° at 0.5° min^{-1} in a parallel beam geometry.

HAXPES measurements were collected at beamline I09 at the Diamond Light Source facility, UK in a standard ultrahigh vacuum (UHV) chamber with a pressure of $<1 \times 10^{-10}$ mbar. A Si(004) channel-cut crystal, following a double-crystal Si(111) monochromator, was used to select x-rays from the source ($h\nu$ = 5.921 keV). Measurements were made using a Scienta Omicron

EW4000 high-energy analyzer with an acceptance angle of ±28°. Calibration was performed using a gold sample, enabling an energy resolution of 0.25 eV to be determined by fitting the Fermi edge with a Fermi–Dirac function convolved with a Gaussian peak. The uncertainty in energies from HAXPES is ±0.03 eV for core level peaks.

XPS measurements were performed in a standard UHV chamber with a pressure of $\sim 1 \times 10^{-10}$ mbar. Surface contaminants were removed by sputtering with Ar^+ ions at a 0.3 kV accelerating voltage. The XPS measurements were taken using a SPECS monochromatic Al Kα X-ray source ($h\nu = 1.487$ keV) operating at 250 W and a hemispherical PSP Vacuum Technology electron-energy analyzer operating with a typical pass energy of 10 eV. The SEC measurements were taken with reduced power (9 W), reduced slit size in the analyser, and a −10 V bias applied. Calibration was performed using a silver sample, enabling an energy resolution of 0.4 eV to be determined by fitting the Fermi edge data. The uncertainty in energies from XPS is ±0.05 eV for core level peaks and ±0.10 eV for VBM positions.

Electronic-structure calculations were performed on the orthorhombic *Pnma* phases of GeS and GeSe using periodic density-functional theory (DFT) as implemented in the Vienna *Ab initio* Simulation Package (VASP) code.[60] The electronic structures were modelled using a plane-wave basis set with a kinetic-energy cutoff of 550 eV and Γ-centered Monkhorst–Pack *k*-point meshes[61] with 7 × 3 × 9 subdivisions (we note that the axes in the simulation structures are oriented such that $b > a > c$, which differs from the orientation shown in Fig. 1). These parameters were chosen to converge the total energy and external pressure to <1 meV per atom and <1 kbar (0.1 GPa) respectively. The ion cores were modelled using projector

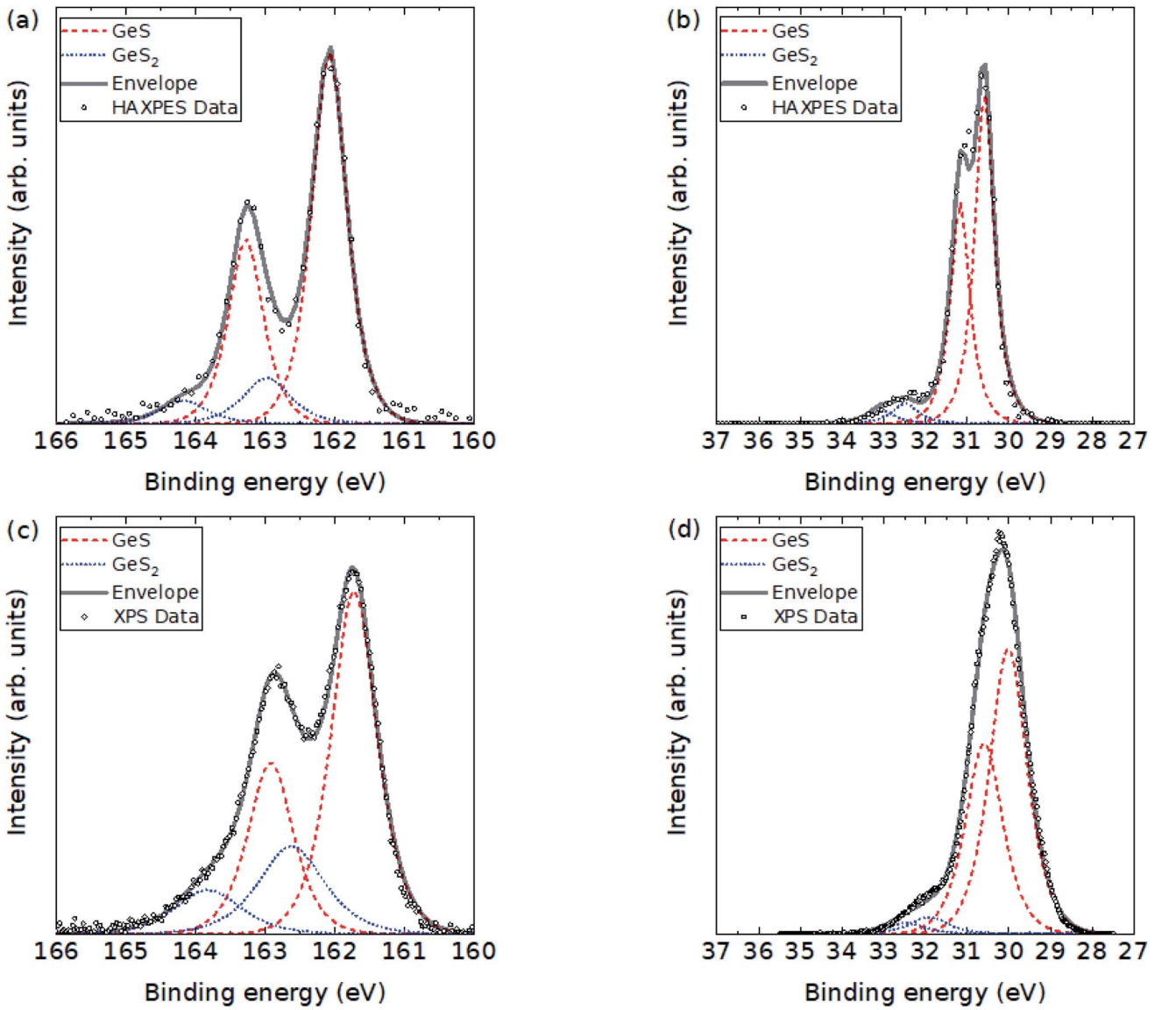

Fig. 3 Photoemission measurements on GeS crystals. (a and b) HAXPES measurements of the S 2p (a) and Ge 3d (b) core levels. (c and d) XPS measurements of the S 2p (c) and Ge 3d (d) core levels. A Shirley background has been subtracted from all four spectra. The peak positions and FWHM are summarised in Table 1.

Table 1 Peak positions (FWHM) from the GeS measurements shown in Fig. 3. The doublet separations for the S 2p and Ge 3d features are 1.2 eV and 0.58 eV respectively. The separation between components associated with the different chemical environments are supported by the fits of more heavily contaminated samples in Fig. S5 and the related information in Table S2

Regions	HAXPES	XPS
S $2p_{3/2}$–GeS	162.1 (0.6)	161.7 (0.8)
S $2p_{3/2}$–GeS_2	163.0 (0.8)	162.6 (1.1)
Ge $3d_{5/2}$–GeS	30.6 (0.5)	30.0 (1.0)
Ge $3d_{5/2}$–GeS_2	32.5 (0.7)	31.9 (1.1)

augmented-wave (PAW) pseudopotentials.[62,63] We tested two different potentials for Ge: one including the Ge 4s, 4p and 3d electrons in the valence region, and one including just the outermost 4s and 4p electrons (*i.e.* treating the Ge 3d electrons as core states). For S and Se, pseudopotentials including the S 3s/3p and Se 4s/4p electrons in the valence region were used.

Geometry optimisations were performed using the PBEsol exchange–correlation functional[64] with the DFT-D3 dispersion correction,[64] *i.e.* PBEsol + D3. The electronic structure was optimised to a tolerance of 10^{-8} eV on the total energy while the atomic positions and lattice parameters were optimised to a tolerance of 10^{-2} eV $Å^{-1}$ on the atomic forces. A Gaussian smearing with a width $\sigma = 0.01$ eV was used to integrate the Brillouin zone.

High-quality electronic-structure calculations were performed on the optimised structures using the HSE06 hybrid functional.[65] These were used to obtain atom- and orbital-projected density-of-states (pDoS) curves and to compute electron-localization functions (ELFs).[66] During these

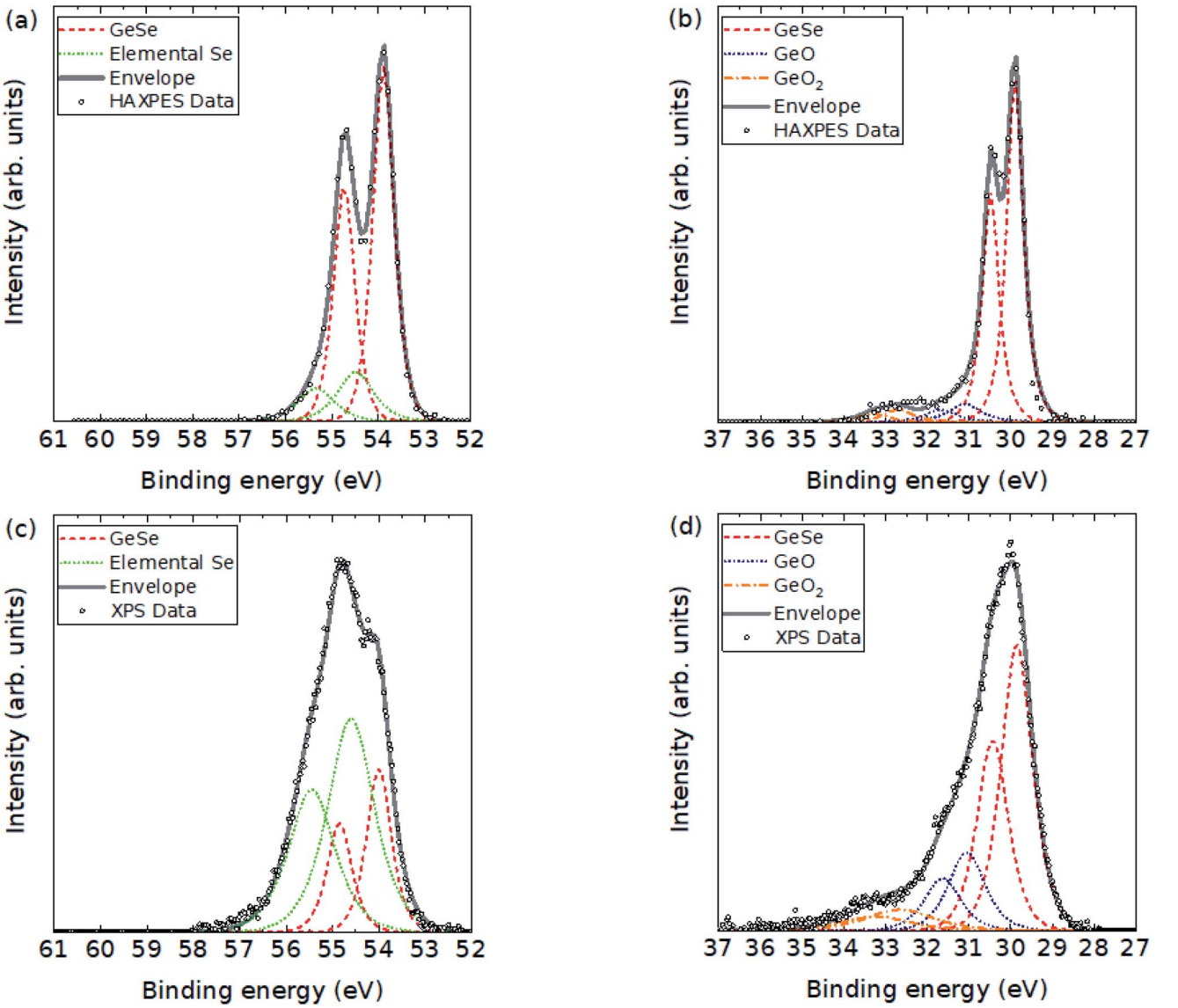

Fig. 4 Photoemission measurements of GeSe crystals. (a and b) HAXPES measurements of the Se 3d (a) and Ge 3d (b) core levels. (c and d) XPS measurements of the Se 3d (c) and Ge 3d (d) core levels. A Shirley background has been subtracted from all four spectra. The peak positions and FWHM are summarised in Table 2.

calculations the tetrahedron method with Blöchl corrections was used for Brillouin-zone integrations,[67] and the number of electronic bands was adjusted to at least twice the number of valence electrons (*i.e.* equal numbers of occupied and virtual states).

In all calculations, the PAW projection was performed in reciprocal space, aspherical contributions to the gradient corrections inside the PAW spheres were accounted for, and the precision of the charge-density grids was set automatically to avoid aliasing errors.

3 Results and discussion

The GeSe bulk crystals used in this experiment are from the same samples investigated in previous work,[14] the structures of which were confirmed by X-ray diffraction and Raman spectroscopy. XRD of the GeS crystals was performed to confirm that the target material had successfully been grown (Fig. S2†).

3.1 Core levels

Fig. 3(a) and (b) show HAXPES measurements on GeS in the S 2p and Ge 3d regions, respectively, while Fig. 3(c) and (d) show equivalent XPS measurements. The positions and full widths at half maxima (FWHM) of the fitted peaks are presented in Table 1. Evidence confirming the absence of oxygen contamination and measurements of the Ge 2p region are given in Fig. S3 and S4† respectively, with related information in Table S1.† One previous study of GeS crystals reported the GeS S $2p_{3/2}$ peaks to be in the region of 161.8 eV, which is in reasonable agreement with our findings.[68] However, previous measurements of the core levels in GeS were unable to clearly resolve the $3d_{5/2}$ and $3d_{3/2}$ components of the Ge 3d doublet due to insufficient resolution.[68,69] This is also the case for our XPS measurements, but we were able to resolve the components using our higher-resolution HAXPES measurements.

HAXPES and XPS measurements of the Se 3d and Ge 3d core levels in GeSe are presented in Fig. 4, and the positions and FWHM of the fitted peaks are presented in Table 2. Measurements of the Ge 2p region are presented in Fig. S6† with related information in Table S3.† Previous studies of GeSe did not report the Se 3d doublet separation.[68,70,71] Previous reports that resolved the Ge 3d doublets place the Ge $3d_{5/2}$ feature at 29.85 eV, in agreement with our findings.[20,71] However, these studies were performed using XPS and therefore lack the energy resolution of our HAXPES measurements.

For GeS, the results indicate a small amount of contamination with GeS_2. As the contamination is visible in the photoemission spectra but not the XRD measurements, this indicates the contamination is limited to the surface. This is not expected to influence the ionization potential (IP) results reported below, due to its low intensity and the significantly higher IP of GeS_2 compared with that of GeS. For GeSe, measurements of the Ge 3d region show GeO and GeO_2. The measurements of the Se 3d region also show some contamination with elemental Se. Only small amounts are detected in the HAXPES spectra, whereas in the XPS measurements the elemental Se component is larger than the GeSe component. The elemental Se component therefore likely corresponds to selenium ejected to the surface when the germanium is oxidised. That the contamination is limited to the surface is again confirmed by the fact that the species are only observed in the photoemission spectra and not in the XRD measurements.

Table 2 Peak positions (FWHM) from the GeSe measurements shown in Fig. 4. The doublet separations for the Se 3d and Ge 3d regions are 0.85 eV and 0.58 eV respectively. The separations between components associated with different chemical environments are supported by the fits of more heavily contaminated samples in Fig. S7 and the related information in Table S4

Regions	HAXPES	XPS
Se $3d_{5/2}$–GeSe	53.9 (0.5)	54.0 (0.6)
Se $3d_{5/2}$–El. Se	54.5 (0.9)	54.6 (1.2)
Ge $3d_{5/2}$–GeSe	29.9 (0.5)	29.9 (0.9)
Ge $3d_{5/2}$–GeO	31.1 (0.9)	31.1 (1.0)
Ge $3d_{5/2}$–GeO_2	32.7 (0.8)	32.7 (1.9)

3.2 Ionisation potentials

Fig. 5(a) and (b) show XPS measurements of the VBM and SEC for GeS and GeSe respectively. These results can be used to calculate the ionization potential (IP) using the equation:

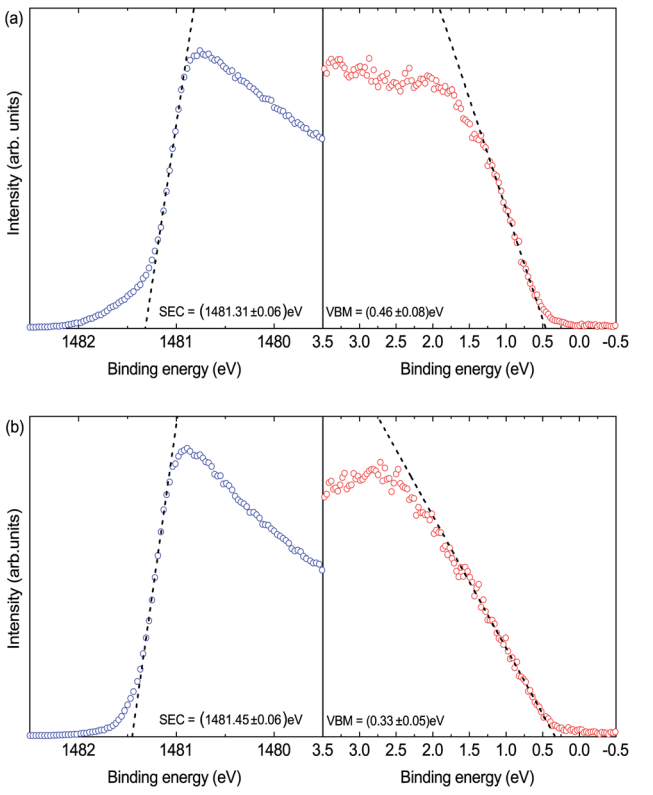

Fig. 5 Secondary electron cutoff (SEC) and valence band onset of GeS (a) and GeSe (b) measured using XPS ($h\nu$ = 1.487 keV). The linear extrapolations used to determine the secondary electron cutoff and valence band maxima are shown by dotted lines.

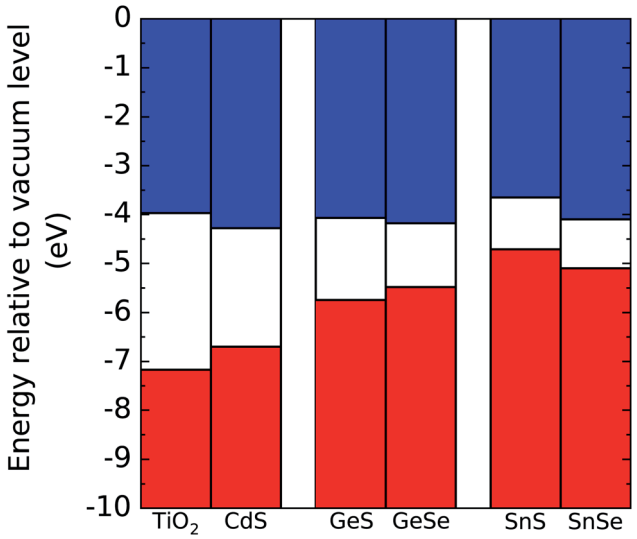

Fig. 6 Comparison of the natural band alignments of GeS and GeSe with some potential window layers for photovoltaic devices. The positions of the valence band maxima of GeS and GeSe were experimentally determined using the measurements in Fig. 5, and the conduction band minima were then inferred from the reported band gaps.[14,15] The band alignments for the window layer materials are taken from the literature.[26,28,73,74]

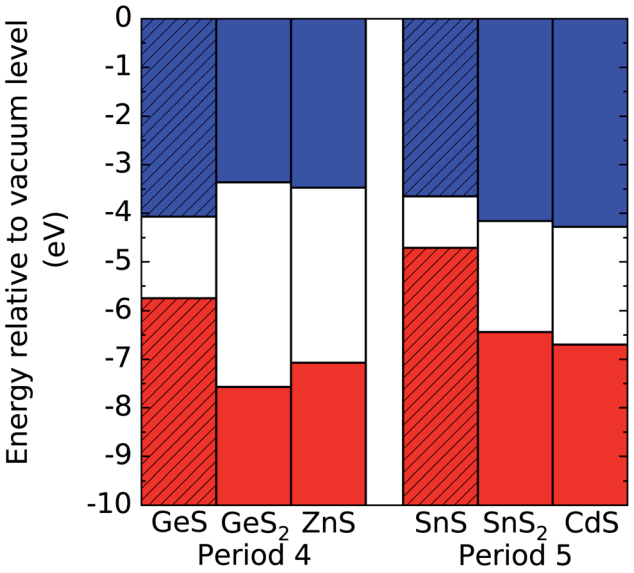

Fig. 7 Comparison of the positions of the valence band maximum (VBM) and conduction band minimum (CBM) of GeS to other Period 4/5 sulphides. The position of the VBM of GeS was determined from the measurements in Fig. 5, and the position of the CBM was determined using the reported band gap.[15] The band positions of the other materials are taken from the literature.[28,73,75,76] The shaded bars used for GeS and SnS indicate that these materials have stereochemically active lone pairs.

$$\mathrm{IP} = h\nu - (\mathrm{SEC} - \mathrm{VBM}). \quad (1)$$

where $h\nu = 1.487$ keV is the energy of the incident x-rays. The IP values were found to be 5.74 eV for GeS and 5.48 eV for GeSe. Using these IP values and literature measurements of the band gaps,[14,15] the positions of the valence and conduction bands of GeS and GeSe were determined and are shown in Fig. 6. The GeSe IP value measured here is similar to, albeit slightly higher than, the 5.12 eV reported previously.[72]

A useful comparison to make is the natural band alignments with potential window layers when using GeS and GeSe in a solar cell (Fig. 6). A number of window layers for GeSe have been proposed theoretically and tested experimentally. TiO_2 is widely used as a window layer in Sb_2Se_3 solar cells.[77] The natural band alignments of TiO_2 with both GeS and GeSe suggest a small spike-like barrier. However, the GeSe/TiO_2 devices reported to date have shown poor performance.[78,79] On the other hand, CdS would exhibit a small cliff-like barrier, and GeSe/CdS devices have shown superior performance to date.[20,71] Given how small the CBOs are for both CdS and TiO_2, the natural band alignments suggest both could be suitable window layers for GeS and GeSe. Theoretical studies have suggested SnS and SnSe as potential partner layers for GeSe-based PV devices.[80,81] For SnS, the natural band alignments with both GeS and GeSe indicate a large cliff-like barrier, which would limit the device efficiency. This could explain why Mao *et al.* observed superior performance in GeSe-based solar cells when partnering with SnSe rather than SnS, as SnSe has an almost flat conduction band alignment with GeSe.[81]

In Fig. 7, the GeS band positions are compared to those of related sulfides to demonstrate the impact the Ge lone pair on the ionisation potentials. This is limited to sulfides because reliable literature data for other selenides appears to be lacking. By comparing to the other Period 4 cation materials, it is clear that the GeS lone pair significantly reduces the ionisation potential. GeS_2 has the same composition and hence valence orbitals, but with Ge in the 4+ rather than +2 oxidation state. ZnS has an almost identical electronic configuration and +2 oxidation state, but no stereochemically active lone pair. Fig. 7 also compares the band positions of the corresponding Period 5 sulphides (*i.e.* GeS and SnS, GeS_2 and SnS_2, ZnS and CdS). This wider comparison again confirms that the presence of the stereochemically active lone pair leads to a marked reduction in the ionisation potential, for both Period 4 and 5 sulphides.

The effect of the lone pair on raising the VBM and reducing the ionisation potential can be understood using the revised lone pair model.[17] The Ge 4s/Sn 5s states hybridise with the S 3p states to form bonding and antibonding states, with the latter being raised above the S 3p states that would otherwise have dominated the VBM and determined the ionisation potential. We have previously demonstrated this for the Sn chalcogenides,[28] and our results show the same effect for GeS. In GeS_2/ZnS and SnS_2/CdS, the antibonding states do not form, and so the ionisation potential is dominated by the S 3p states, which are at higher binding energy, and thus these materials have lower valence band maxima and higher ionisation potentials.

3.3 Valence band spectra

From our DFT calculations we obtained optimised lattice constants of $a = 10.229$, $b = 3.643$ and $c = 4.150$ Å for GeS and

$a = 10.783$, $b = 3.848$ and $c = 4.352$ Å for GeSe, which differ by at most 3.6% from the experimental measurements.[14,18] Using the HSE06 hybrid functional[65] we calculated direct and indirect band gaps of 1.68/1.35 and 1.35/1.19 eV for GeS and GeSe, respectively, the former of which compare very favourably to the measured direct gaps of 1.6 and 1.33 eV.[14,15] Both sets of values were obtained using pseudopotentials treating the Ge 3d electrons as valence states, similar to the potentials used in our previous work on the tin sulfides.[24,28] Treating the 3d electrons instead as core states changed the optimised lattice parameters by 0.1–0.6% and the calculated band gaps by 2–33 meV (see ESI, Tables S5 and S6†). The largest difference in the band gaps was a 2.8% reduction in the calculated indirect gap of GeSe. The different treatments of the Ge 3d states also had a minimal effect on the calculated pDoS curves (see ESI Fig. S9 and S10†).

Fig. 8 compares the valence band photoemission spectra measured using XPS and HAXPES to pDoS curves obtained from hybrid DFT. Fig. 8(a) and (b) show the HAXPES and XPS results for GeS, respectively, while Fig. 8(c) and (d) show the same data for GeSe. The calculated pDoS are weighted using the relevant one electron photoionisation cross sections (Fig. 2)[22] and convolved with a Gaussian function to account for instrumental and thermal broadening and a Lorentzian function to account for lifetime broadening. The FWHM of the Gaussian functions were 0.24 eV and 0.38 eV for the HAXPES and XPS simulations, respectively, while the FWHM of the Lorentzian functions were 0.24 eV and 0.30 eV. Calculated pDoS curves without cross-section correction and broadening are shown in Fig. S8.†

For GeS, the HAXPES measurements in Fig. 8(a) begin with a narrow peak at the VBM (0–2.5 eV), followed by a plateau to 6–

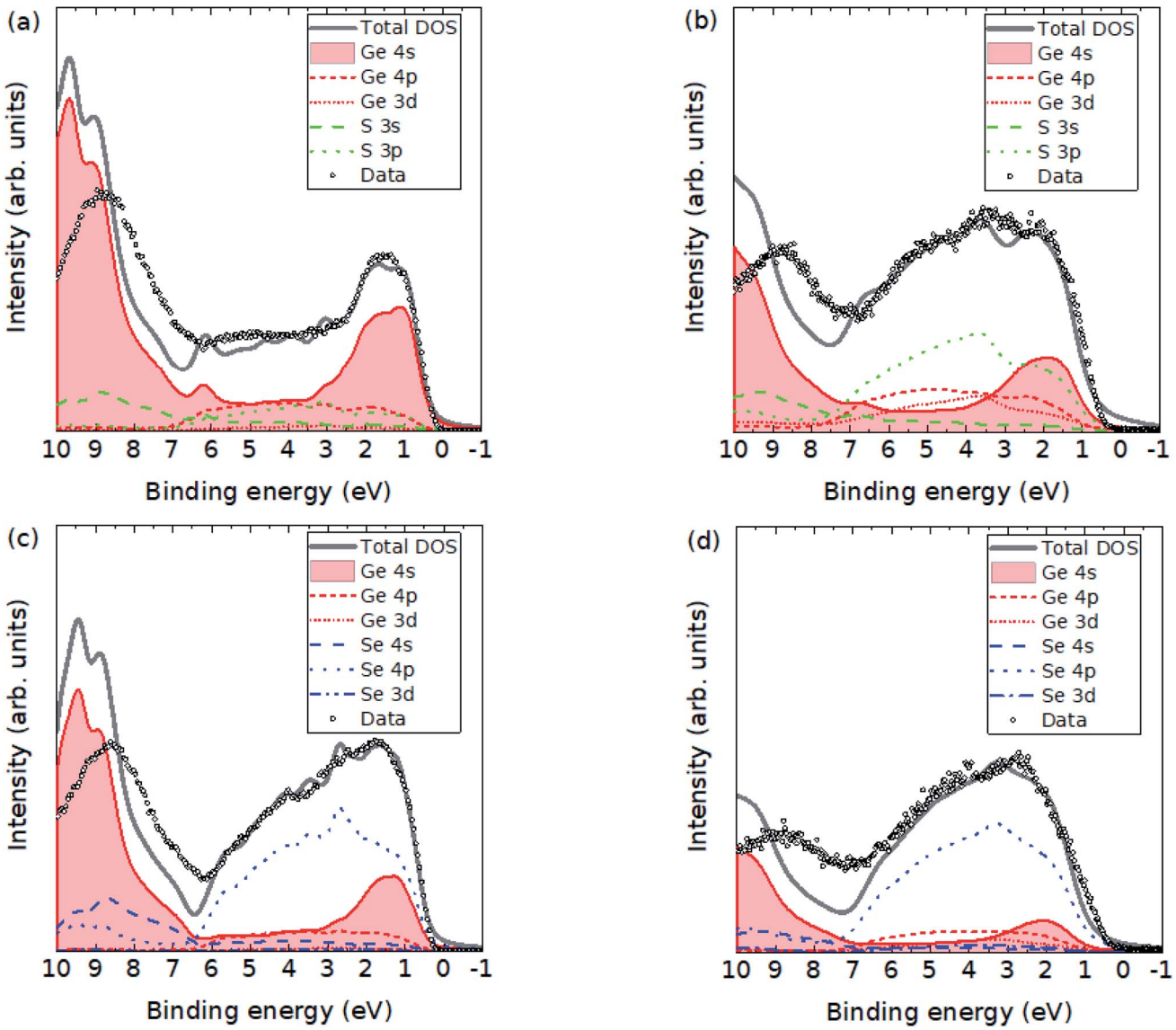

Fig. 8 Comparison of the experimental valence band spectra of GeS and GeSe to the atom- and orbital-projected electronic density of states (pDoS) curves obtained from hybrid DFT calculations. (a) and (b) compare the HAXPES and XPS measurements on GeS, respectively. (c) and (d) compare the same data for GeSe. All four plots compare the measurements to the DFT pDoS after weighting with the cross sections in Fig. 2.

7 eV and a broad peak centred around 9 eV. In the XPS measurements in Fig. 8(b), there is instead one broad peak from the VBM (0–6 eV) followed by a second peak centred around 8.5 eV. The differences between the two spectra are explained well by the calculated cross-section corrected pDoS curves, with experiment and theory agreeing well up to around 7 eV. The broad peak in the XPS data is shown to be composed of contributions from S 3p and Ge 4s, 4p and 3d orbitals, together with a small contribution from S 3s states. However, as expected from the one-electron photoionisation cross sections, the Ge 4s orbitals make a more significant contribution to the HAXPES spectra than the other orbitals, and the more pronounced peak therefore arises from the presence of the Ge 4s states at the VBM. This provides experimental evidence, for the first time, for the presence of Ge 4s states at the VBM in GeS, which is an important indicator of the cation having a stereochemically active lone pair. This also provides direct evidence to support our explanation of the comparatively low ionisation potential of GeS demonstrated in Fig. 7.

Both the HAXPES and XPS measurements on GeSe in Fig. 8(c) and (d), respectively, begin with one broad peak from the VBM (0–7 eV) followed by a second smaller peak centred around 9 eV. However, there are subtle differences in the shapes of the two broad peaks. The valence band has a sharper onset in the HAXPES than in the XPS spectra, and the top of the first broad peak is closer to the onset in the former. This subtle difference in shape is again explained by the calculated pDoS curves, and the experiments and theory again agree well up to 7 eV. The subtle differences are related to the hybridised lone pair states present at the VBM. The XPS peak shows a large contribution from Se 4p orbitals, with the height of the experimental valence band spectrum close to the maximum of the Se 4p pDoS. The broad peak also contains smaller contributions from the Ge 4s, 4p and 3d and the Se 4s and 4p states. As expected from the differences in the cross sections, the Ge $4s^2$ orbitals make a larger contribution to the HAXPES than to the XPS spectra. This causes the sharper onset at the valence band, where the Ge 4s orbitals contribute to the density of states, and shifts the maximum of the broad peak closer to the onset. Once again, this provides the first experimental evidence for the presence of Ge 4s orbitals at the VBM in GeSe, and hence evidence for stereochemically active lone pairs.

A noteworthy feature of all four comparisons in Fig. 8 is the divergence between experiment and theory at higher binding energies, which is a relatively common occurrence.[82,83] A possible cause of this is that the cross-section corrected DFT valence band DOS are based on the ground-state electronic structure whereas the experimental spectra probe the materials in an excited state. Ley *et al.* state that this will shift experimental features toward the top of the valence band relative to spectra predicted from theory, which is consistent with how our measurements and calculations compare.[84]

The key finding from the present analysis is the presence of Ge 4s orbitals at the valence band edge in both GeS and GeSe. The revised lone pair model indicates that in order for these stereochemically active lone pairs to form the Ge 4s orbitals must interact with the anion S 3p/Se 4p orbitals to form bonding and antibonding states. The presence of the Ge 4s states at the valence band edges is, therefore, evidence that the antibonding states predicted by the revised lone pair model are present, and hence that these materials have the stereochemically active lone pairs found in several other high-performance PV materials. The formation of these bonding and antibonding states is only possible in a distorted crystal structure, because the orbital interactions would otherwise be forbidden by symmetry. The asymmetric electron densities associated with the distorted orthorhombic crystal structures thus arise from the stabilisation of the Ge $4s^2$ lone pairs.

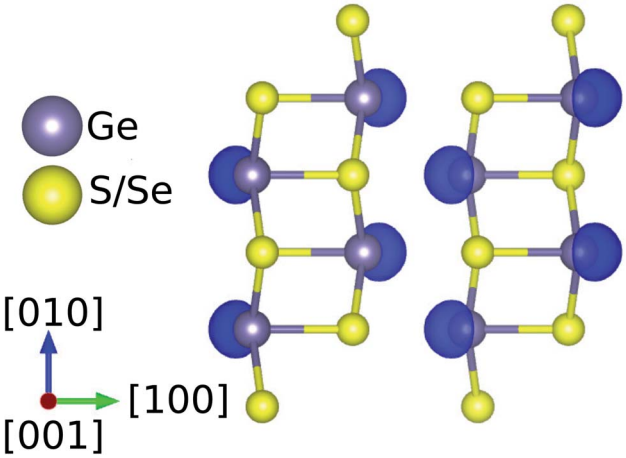

Fig. 9 Electron localisation function for GeS obtained using hybrid DFT (isosurface level: 0.918), showing the Ge 4s lone pair in blue. Similar results are obtained for GeSe – see ESI Fig. S12.† This image was prepared using the VESTA software.[8]

The Ge lone pairs in GeS and GeSe can be visualised using the electron localisation function (ELF)[66] isosurfaces (Fig. 9). The lone pairs are seen to project between the nanosheets in the [100] direction, which is typical of stereochemically active lone pairs and the associated crystal structure distortions. The ELF shown in Fig. 9 was generated from the calculations where the Ge 3d electrons were treated as core states. Despite the very similar electronic structures, we found that including these states in the valence region led to a notably more spherical charge density around the Ge atoms and substantial delocalization of the Ge lone pair (see ESI Fig. S11–S14†). Despite this, as noted above we found no significant differences in the pDoS, including in the contributions of the Ge 4s states to the VBM, and we also found no significant differences in the atomic charges and volumes obtained from topological analyses of the charge densities[85] (see ESI Fig. S9/S10 and Tables S7/S8†). We are therefore unsure of whether this discrepancy is simply an artefact in the calculations.

When comparing the pDoS of GeS and GeSe it is clear that the Ge 4s orbitals make a larger contribution to the valence band edge in GeS than in GeSe. As shown in Fig. 10(a), the S 3p has a lower configuration energy than the Se 4p, which means the separation between the Ge 4s states and the anion p states is smaller in GeS than in GeSe.[86] This means that when the Ge 4s and the anion p states interact to form bonding and antibonding

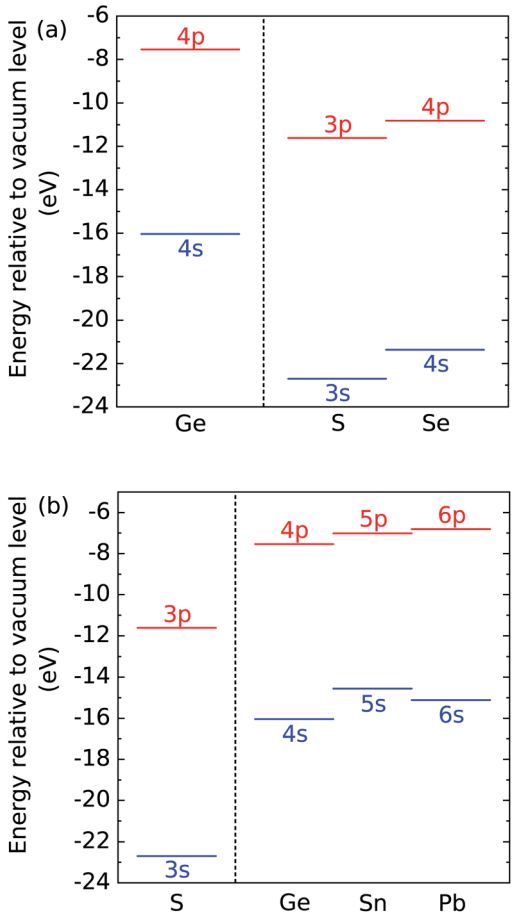

Fig. 10 Experimentally determined electronic configuration energies of the valence s and p orbitals in Ge, Sn, Pb, S and Se atoms using data from ref. 86 and 92. (a) Comparison of the energies of Ge with those of S and Se. (b) Comparison the energies of S with those of Ge, Sn and Pb. In the revised lone pair model, the energy separation between the cation s and anion p levels is a key descriptor of the strength of the interactions that drive the formation of active lone pairs and the resulting structural distortions.

states, the Ge 4s make a larger contribution to the antibonding states that form the valence band edge in GeS than in GeSe. This analysis was first performed by Watson *et al.* for Pb 6s lone pairs.[87] Waghmare *et al.* subsequently used DFT calculations to evidence this phenomenon for other cubic IV–VI chalcogenides, including GeS and GeSe, but the cubic compounds do not allow for lattice distortion.[42] The phenomenon was later generalised by Walsh *et al.* with the revised lone pair model.[17] The pattern of the Ge lone pair making a larger contribution to the antibonding states as the size of the anion decreases is consistent with previous studies on Sn and Sb lone pairs.[88,89]

A further finding from this work is therefore that the Ge^{2+} cation can form stereochemically active lone pairs. This finding should offer new avenues in fields beyond the Ge chalcogenides – for example, research into Ge perovskites may also benefit from confirmation that the lone pair formation is possible, despite the additional challenges posed by oxidation.[10,51–53,59,90] The traditional lone pair model has generally disregarded $4s^2$ lone pairs as it was assumed that d-block (scandide) contractions would dominate in this row of the periodic table.[91] Similarly, the revised lone pair model predicts that the formation of stereochemically active lone pairs in GeS and GeSe is unlikely due to the difference in energy between the Ge 4s and S 3p/Se 4p atomic levels.

As can be seen in Fig. 10(b), the difference between the Ge 4s and S 3p states is greater than the difference between the Pb 6s and S 3p states. PbS is known to have an inactive lone pair, and the revised lone pair model explains this by the separation between anion p and cation s states being too large to form the asymmetric electron density required to drive the structural distortion. Using the same logic, the formation of the distorted GeS structure then seems highly unlikely as the difference between the states is larger still. As it is clear from the present studies that a stereochemically active lone pair does form, we propose a potential addendum to the model: since Ge is smaller than Pb, one might explain the different behaviour by taking into account the bond length between the cation and anion, as Orgel has suggested previously.[93,94]

We attempted to investigate the influence of the Ge–chalcogen bond length on the lone pair activity in GeS and GeSe by performing further electronic-structure calculations with the unit-cell volume of both systems adjusted to ±10% of the equilibrium volume V_{eq} (Fig. S15–S19†). We found that the cell axis corresponding to the strongest bonding direction is resistant to change under compression and expansion, such that there is little variation in the nearest-neighbour Ge-chalcogen distance (Fig. S15†). Despite this, there is a large variation in the direct and indirect bandgaps (Fig. S16†). We observe some variation in the Ge s PDoS in the vicinity of the VBM in both systems, although the integral is largely preserved within a window of ~2.5 eV below the Fermi energy (Fig. S17 and S18†). Most importantly, analysis of the ELFs at compressed and expanded volumes show that the Ge lone pair is retained at all the volumes tested (Fig. S19†). We therefore conclude that fully testing our hypothesis on the importance of the cation–anion distance would require a systematic analysis of different chemical systems (*i.e.* different structural phases and/or chemical species), which we consider to be beyond the scope of the present study.

4 Conclusions

In conclusion, germanium sulfide and germanium selenide bulk crystals have successfully been prepared using a melt growth technique. X-ray photoemission spectroscopy has been used to measure the secondary electron cutoffs and valence band offsets to determine ionisation potentials of 5.74 eV and 5.48 eV. The positions of the conduction-band minima were then deduced from the positions of the valence band maxima relative to vacuum level and the reported band gaps. The band alignments were compared to potential window layers for photovoltaic devices, and this comparison suggests CdS and TiO_2 as potential partner materials. Our measurements also clearly show that the ionisation potential of GeS is higher than in comparable materials, which we ascribe to the presence of

stereochemically active lone pairs and the associated antibonding states at the valence band maximum. Using a combination of X-ray photoemission and hard X-ray photoemission spectroscopy, in conjunction with hybrid density-functional theory calculations, we have presented direct evidence for these active lone pairs in both GeS and GeSe, with interesting implications for the revised lone pair model and for related areas of research such as Ge-based perovskites.

Author contributions

Conceptualization by MJS, JMS and TDV. DFT investigation and analysis by JMS. HAXPES investigation by MJS, LAHJ, HS, TJF, JENS, PKT and T-LL. XPS investigation by MJS and HJE. Photoemission analysis by MJS with input from HS. Samples prepared by MJS and PAEM. Instrumentation maintained by LAHJ, HJE, VRD, PKT and T-LL. Supervision by VRD and TDV. Project administration by MJS, JMS and TDV. Manuscript drafted by MJS, JMS and TDV and reviewed and edited by all authors.

Conflicts of interest

There are no conflicts to declare.

Acknowledgements

The Engineering and Physical Sciences Research Council (EPSRC) is acknowledged for providing funding to M. J. S., J. E. N. S, and T. J. F. (Grant No. EP/L01551X/1), H. S. (Grant No. EP/N509693/1), L. A. H. J. (Grant No. EP/R513271/1), and V. R. D. and T. D. V. (Grant No. EP/N015800/1). JMS is supported by a UK Research and Innovation (UKRI) Future Leaders Fellowship (Grant No. MR/T043121/1), and previously held a University of Manchester Presidential Fellowship. The XRD facility was supported by the EPSRC under Grant No. EP/P001513/1. Diamond Light Source is acknowledged for providing beam time on beamline I09 under proposals SI21431-1 and SI23160-1. Computational modelling was performed on the UK Archer high-performance computing facility *via* membership of the UK Materials Chemistry Consortium, which is funded by the EPSRC (Grant No. EP/L000202, EP/R029431).

References

1 M. A. Green, E. D. Dunlop, J. Hohl-Ebinger, M. Yoshita, N. Kopidakis and X. Hao, *Progress in Photovoltaics: Research and Applications*, 2020, **28**, 629–638.
2 C. Candelise, M. Winskel and R. Gross, *Prog. Photovoltaics*, 2012, **20**, 816–831.
3 S. Battersby, *Proc. Natl. Acad. Sci. U. S. A.*, 2019, **116**, 7–10.
4 M. Birkett, W. M. Linhart, J. Stoner, L. J. Phillips, K. Durose, J. Alaria, J. D. Major, R. Kudrawiec and T. D. Veal, *APL Mater.*, 2018, **6**, 084901.
5 Z. Li, X. Liang, G. Li, H. Liu, H. Zhang, J. Guo, J. Chen, K. Shen, X. San, W. Yu, R. E. I. Schropp and Y. Mai, *Nat. Commun.*, 2019, **10**(125), 1–9.
6 Y. Zhou, L. Wang, S. Chen, S. Qin, X. Liu, J. Chen, D.-J. Xue, M. Luo, Y. Cao, Y. Cheng, E. H. Sargent and J. Tang, *Nat. Photonics*, 2015, **9**, 409–415.
7 L. Wang, D. B. Li, K. Li, C. Chen, H. X. Deng, L. Gao, Y. Zhao, F. Jiang, L. Li, F. Huang, Y. He, H. Song, G. Niu and J. Tang, *Nat. Energy*, 2017, **2**, 17046.
8 K. Momma and F. Izumi, *J. Appl. Crystallogr.*, 2011, **44**, 1272–1276.
9 C. H. Don, H. Shiel, T. D. C. Hobson, C. N. Savory, J. E. N. Swallow, M. J. Smiles, L. A. H. Jones, T. Featherstone, P. K. Thakur, T. L. Lee, K. Durose, J. D. Major, V. Dhanak, D. O. Scanlon and T. D. Veal, *J. Mater. Chem. C*, 2020, **8**, 12615–12622.
10 A. M. Ganose, C. N. Savory and D. O. Scanlon, *Chem. Commun.*, 2017, **53**, 20–44.
11 D. H. Fabini, R. Seshadri and M. G. Kanatzidis, *MRS Bull.*, 2020, **45**, 467–477.
12 R. E. Brandt, V. Stevanovic, D. S. Ginley and T. Buonassisi, *MRS Commun.*, 2015, **5**, 275.
13 G. W. C. Kaye, T. H. Laby, J. G. Noyes, G. F. Phillips, O. Jones and J. Asher, *Tables of Physical & Chemical Constants, 16th edition, 1995*, Section 3.1.3 Abundances of the elements, Kaye & Laby Online, Version 1.0 (2005), https://web.archive.org/web/20190518224615/http://www.kayelaby.npl.co.uk/chemistry/3_1/3_1_3.html, accessed Feb 11, 2021.
14 P. A. E. Murgatroyd, M. J. Smiles, C. N. Savory, T. P. Shalvey, J. E. N. Swallow, N. Fleck, C. M. Robertson, F. Jäckel, J. Alaria, J. D. Major, D. O. Scanlon and T. D. Veal, *Chem. Mater.*, 2020, **32**, 3245–3253.
15 P. Ramasamy, D. Kwak, D. H. Lim, H. S. Ra and J. S. Lee, *J. Mater. Chem. C*, 2016, **4**, 479–485.
16 W. Shockley and H. J. Queisser, *J. Appl. Phys.*, 1961, **32**, 510–519.
17 A. Walsh, D. J. Payne, R. G. Egdell and G. W. Watson, *Chem. Soc. Rev.*, 2011, **40**, 4455–4463.
18 W. H. Zachariasen, *Phys. Rev.*, 1932, **40**, 917–922.
19 A. Okazaki, *J. Phys. Soc. Jpn.*, 1958, **13**, 1151–1155.
20 S.-C. Liu, C.-M. Dai, Y. Min, Y. Hou, A. H. Proppe, Y. Zhou, C. Chen, S. Chen, J. Tang, D.-J. Xue, *et al.*, *Nat. Commun.*, 2021, **12**, 670.
21 M. Feng, S-C. Lui, J. Wu, X. Liu, D-J. Xue, J-S. Hu and L-J. Wan, *J. Am. Chem. Soc.*, 2021, **143**, 9664–9671.
22 J. H. Scofield, *Theoretical photoionization cross sections from 1 to 1500 keV*, 1973.
23 P. Day, *Electronic Structure and Magnetism of Inorganic Compounds*, Royal Society of Chemistry, 2007, vol. 3.
24 L. A. H. Jones, W. M. Linhart, N. Fleck, J. E. N. Swallow, P. A. E. Murgatroyd, H. Shiel, T. J. Featherstone, M. J. Smiles, P. K. Thakur, T. L. Lee, L. J. Hardwick, J. Alaria, F. Jäckel, R. Kudrawiec, L. A. Burton, A. Walsh, J. M. Skelton, T. D. Veal and V. R. Dhanak, *Phys. Rev. Mater.*, 2020, **4**, 074602.
25 D. J. Payne, R. G. Egdell, D. S. L. Law, P.-A. Glans, T. Learmonth, K. E. Smith, J. Guo, A. Walsh and G. W. Watson, *J. Mater. Chem.*, 2007, **17**, 267–277.

26 H. Shiel, O. S. Hutter, L. J. Phillips, J. E. N. Swallow, L. A. H. Jones, T. J. Featherstone, M. J. Smiles, P. K. Thakur, T.-L. Lee, V. R. Dhanak, J. D. Major and T. D. Veal, *ACS Appl. Energy Mater.*, 2020, **3**, 11617–11626.
27 T. D. Veal, D. O. Scanlon, R. Kostecki and E. Arca, *J. Phys.: Energy*, 2021, **3**, 032001.
28 T. J. Whittles, L. A. Burton, J. M. Skelton, A. Walsh, T. D. Veal and V. R. Dhanak, *Chem. Mater.*, 2016, **28**, 3718–3726.
29 J. D. Wiley, W. J. Buckel, W. Braun, G. W. Fehrenbach, F. J. Himpsel and E. E. Koch, *Phys. Rev. B: Solid State*, 1976, **14**, 697–701.
30 A. Kosakov, H. Neumann and G. Leonhardt, *J. Electron Spectrosc. Relat. Phenom.*, 1977, **12**, 181–189.
31 R. B. Shalvoy, G. B. Fisher and P. J. Stiles, *Phys. Rev. B: Solid State*, 1977, **15**, 2021–2024.
32 P. C. Kemeny, J. Azoulay, M. Cardona and L. Ley, *Il Nuovo Cimento*, 1977, **39B**, 709–714.
33 G. D. Davis, P. E. Viljoen and M. G. Lagally, *J. Electron Spectrosc. Relat. Phenom.*, 1980, **21**, 135–152.
34 S. Hino, T. Takahashi and Y. Harada, *Solid State Commun.*, 1980, **35**, 379–382.
35 E. O'Reilly, J. Robertson and M. Kelly, *Solid State Commun.*, 1981, **38**, 565–568.
36 E. P. O'Reilly, *J. Phys. C: Solid State Phys.*, 1982, **15**, 1449–1455.
37 T. Takahashi and T. Sagawa, *J. Non-Cryst. Solids*, 1982, **53**, 195–199.
38 J. Robertson and E. P. O'Reilly, *Philos. Mag. B*, 1983, **47**, 621–626.
39 T. Takahashi and T. Sagawa, *J. Non-Cryst. Solids*, 1983, **59–60**, 879–882.
40 F. M. Gashimzade, D. G. Guliev, D. A. Guseinova and V. Y. Shteinshrayber, *J. Phys.: Condens. Matter*, 1992, **4**, 1081–1091.
41 S. Hosokawa, Y. Hari, T. Kouchi, I. Ono, H. Sato, M. Taniguchi, A. Hiraya, Y. Takata, N. Kosugi and M. Watanabe, *J. Phys.: Condens. Matter*, 1998, **10**, 1931–1950.
42 U. V. Waghmare, N. A. Spaldin, H. C. Kandpal and R. Seshadri, *Phys. Rev. B: Condens. Matter Mater. Phys.*, 2003, **67**, 125111.
43 D. I. Bletskan, K. E. Glukhov and V. M. Kabatsii, *J. Optoelectron. Adv. Mater.*, 2019, **21**, 629–640.
44 X. Kong, J. Deng, L. Li, Y. Liu, X. Ding, J. Sun and J. Z. Liu, *Phys. Rev. B*, 2018, **98**, 184104.
45 S. Jia, H. Li, T. Gotoh, C. Longeaud, B. Zhang, J. Lyu, S. Lv, M. Zhu, Z. Song, Q. Liu, J. Robertson and M. Liu, *Nat. Commun.*, 2020, **11**, 4636.
46 J.-V. Raty and M. Wuttig, *J. Phys. D: Appl. Phys.*, 2020, **53**, 234002.
47 L. Makinistian and E. A. Albanesi, *J. Phys.: Condens. Matter*, 2007, **19**, 186211.
48 P. Mishra, H. Lohani, A. K. Kundu, R. Patel, G. K. Solanki, K. S. R. Menon and B. R. Sekhar, *Semicond. Sci. Technol.*, 2015, **30**, 075001.
49 S. N. Dutta and G. A. Jeffrey, *Inorg. Chem.*, 1965, **4**, 1363–1366.
50 M. Sist, C. Gatti, P. Nørby, S. Cenedese, H. Kasai, K. Kato and B. B. Iversen, *Chem.–Eur. J.*, 2017, **23**, 6888–6895.
51 A. Walsh, *J. Phys. Chem. C*, 2015, **119**, 5755–5760.
52 D. B. Mitzi, *Chem. Mater.*, 1996, **8**, 791–800.
53 T. Krishnamoorthy, H. Ding, C. Yan, W. L. Leong, T. Baikie, Z. Zhang, M. Sherburne, S. Li, M. Asta, N. Mathews and S. G. Mhaisalkar, *J. Mater. Chem. A*, 2015, **3**, 23829–23832.
54 G. Qing-Tian, P. Qi-Wei, S. Wei, S. Xun and F. Chang-Shui, *Prog. Cryst. Growth Charact. Mater.*, 2000, **40**, 89–95.
55 Q. Gu, Q. Pan, X. Wu, W. Shi and C. Fang, *J. Cryst. Growth*, 2000, **212**, 605–607.
56 L. C. Tang, J. Y. Huang, C. S. Chang, M. H. Lee and L. Q. Liu, *J. Phys.: Condens. Matter*, 2005, **17**, 7275.
57 L.-C. Tang, C.-S. Chang, L.-C. Tang and J. Y. Huang, *J. Phys.: Condens. Matter*, 2000, **12**, 9129–9143.
58 Y.-Q. Zhao, L.-J. Wu, B. Liu, L.-Z. Wang, P.-B. He and M.-Q. Cai, *J. Power Sources*, 2016, **313**, 96–103.
59 C. C. Stoumpos, L. Frazer, D. J. Clark, Y. S. Kim, S. H. Rhim, A. J. Freeman, J. B. Ketterson, J. I. Jang and M. G. Kanatzidis, *J. Am. Chem. Soc.*, 2015, **137**, 6804–6819.
60 G. Kresse and J. Hafner, *Phys. Rev. B: Condens. Matter Mater. Phys.*, 1993, **47**, 558–561.
61 H. J. Monkhorst and J. D. Pack, *Phys. Rev. B: Solid State*, 1976, **13**, 5188–5192.
62 P. E. Blöchl, *Phys. Rev. B: Condens. Matter Mater. Phys.*, 1994, **50**, 17953–17979.
63 G. Kresse and D. Joubert, *Phys. Rev. B: Condens. Matter Mater. Phys.*, 1999, **59**, 1758–1775.
64 J. P. Perdew, A. Ruzsinszky, G. I. Csonka, O. A. Vydrov, G. E. Scuseria, L. A. Constantin, X. Zhou and K. Burke, *Phys. Rev. Lett.*, 2008, **100**, 136406.
65 A. V. Krukau, O. A. Vydrov, A. F. Izmaylov and G. E. Scuseria, *J. Chem. Phys.*, 2006, **125**, 224106.
66 B. Silvi and A. Savin, *Nature*, 1994, **371**, 683–686.
67 P. E. Blöchl, O. Jepsen and O. K. Andersen, *Phys. Rev. B: Condens. Matter Mater. Phys.*, 1994, **49**, 16223–16233.
68 R. B. Shalvoy, G. B. Fisher and P. J. Stiles, *Phys. Rev. B: Solid State*, 1977, **15**, 1680–1697.
69 G. Hollinger, P. Kumurdjian, J. Mackowski, P. Pertosa, L. Porte and T. M. Duc, *J. Electron Spectrosc. Relat. Phenom.*, 1974, **5**, 237–245.
70 U. Tokihiro, *Jpn. J. Appl. Phys.*, 1983, **22**, 1349–1352.
71 D.-J. Xue, S.-C. Liu, C.-M. Dai, S. Chen, C. He, L. Zhao, J.-S. Hu and L.-J. Wan, *J. Am. Chem. Soc.*, 2017, **139**, 958–965.
72 R. Li, W. Xia, Y. Guo and J. Xue, *Appl. Phys. Lett.*, 2019, **114**, 013505.
73 T. J. Whittles, T. D. Veal, C. N. Savory, A. W. Welch, F. W. de Souza Lucas, J. T. Gibbon, M. Birkett, R. J. Potter, D. O. Scanlon, A. Zakutayev and V. R. Dhanak, *ACS Appl. Mater. Interfaces*, 2017, **9**, 41916–41926.
74 H. S. Im, Y. Myung, Y. J. Cho, C. H. Kim, H. S. Kim, S. H. Back, C. S. Jung, D. M. Jang, Y. R. Lim, J. Park and J.-P. Ahn, *RSC Adv.*, 2013, **3**, 10349–10354.
75 F. A. Rasmussen and K. S. Thygesen, *J. Phys. Chem. C*, 2015, **119**, 13169–13183.
76 Y. Xu and M. A. Schoonen, *Am. Mineral.*, 2000, **85**, 543–556.

77 L. J. Phillips, C. N. Savory, O. S. Hutter, P. J. Yates, H. Shiel, S. Mariotti, L. Bowen, M. Birkett, K. Durose, D. O. Scanlon and J. D. Major, *IEEE Journal of Photovoltaics*, 2019, **9**, 544–551.
78 B. Chen, Y. Ruan, J. Li, W. Wang, X. Liu, H. Cai, L. Yao, J.-M. Zhang, S. Chen and G. Chen, *Nanoscale*, 2019, **11**, 3968–3978.
79 O. S. Hutter, L. J. Phillips, K. Durose and J. D. Major, *Sol. Energy Mater. Sol. Cells*, 2018, **188**, 177–181.
80 X. Lv, W. Wei, C. Mu, B. Huang and Y. Dai, *J. Mater. Chem. A*, 2018, **6**, 5032–5039.
81 Y. Mao, C. Xu, J. Yuan and H. Zhao, *J. Mater. Chem. A*, 2019, **7**, 11265–11271.
82 S. K. Vasheghani Farahani, T. D. Veal, J. J. Mudd, D. O. Scanlon, G. W. Watson, O. Bierwagen, M. E. White, J. S. Speck and C. F. McConville, *Phys. Rev. B: Condens. Matter Mater. Phys.*, 2014, **90**, 155413.
83 S. Mandal, K. Haule, K. M. Rabe and D. Vanderbilt, *npj Comput. Mater.*, 2019, **5**, 2057–3960.
84 L. Ley, R. A. Pollak, F. R. McFeely, S. P. Kowalczyk and D. A. Shirley, *Phys. Rev. B: Solid State*, 1974, **9**, 600–621.
85 G. Henkelman, A. Arnaldsson and H. Jónsson, *Comput. Mater. Sci.*, 2006, **36**, 354–360.
86 J. B. Mann, T. L. Meek and L. C. Allen, *J. Am. Chem. Soc.*, 2000, **122**, 2780–2783.
87 G. W. Watson, S. C. Parker and G. Kresse, *Phys. Rev. B: Condens. Matter Mater. Phys.*, 1999, **59**, 8481–8486.
88 A. Walsh and G. W. Watson, *J. Phys. Chem. B*, 2005, **109**, 18868–18875.
89 J. J. Carey, J. P. Allen, D. O. Scanlon and G. W. Watson, *J. Solid State Chem.*, 2014, **213**, 116–125.
90 Y.-Q. Zhao, L.-J. Wu, B. Liu, L.-Z. Wang, P.-B. He and M.-Q. Cai, *J. Power Sources*, 2016, **313**, 96–103.
91 P. Pyykko, *Chem. Rev.*, 1988, **88**, 563–594.
92 L. C. Allen, *J. Am. Chem. Soc.*, 1989, **111**, 9003–9014.
93 J. Dunitz and L. Orgel, in *Stereochemistry of Ionic Solids*, ed. H. Emeleus and A. Sharpe, Academic Press, 1960, vol. 2, pp. 1–60.
94 L. E. Orgel, *J. Chem. Soc.*, 1959, 3815–3819.

